



The Fate of Liquid Crystal Topological Defects on Chemically Patterned Surfaces during Phase Transitions

Journal:	<i>Soft Matter</i>
Manuscript ID	SM-ART-05-2022-000566.R1
Article Type:	Paper
Date Submitted by the Author:	01-Jul-2022
Complete List of Authors:	Pawale, Tejal; University of North Texas, Materials science and engineering Yi, Shengzhu; The Hong Kong University of Science and Technology Department of Physics Wang, Xiaowei; University of North Texas Zhang, Rui; The Hong Kong University of Science and Technology Department of Physics Li, Xiao; University of North Texas, Material Science and Engineering

The Fate of Liquid Crystal Topological Defects on Chemically Patterned Surfaces during Phase Transitions

Tejal Pawale^{1#}, Shengzhu Yi^{2,3#}, Xiaowei Wang¹, Rui Zhang^{2*}, Xiao Li^{1*}

1 Materials Science and Engineering Department, University of North Texas, Denton, USA

2 Department of physics, The Hongkong University of Science and Technology, Hongkong, China

3 Department of Mechanical and Energy Engineering, Southern University of Science and Technology, Shenzhen, Guangdong, China.

Equal contribution.

* Corresponding author: Xiao.Li@unt.edu, ruizhang@ust.hk

Abstract:

Controlling topological defects in liquid crystals (LCs) is an essential element in the development of areas such as directed self-assembly and micropatterning materials. However, during the phase transition in confined patterned surfaces, how the morphologies in one liquid crystalline phase change from deformations or defects into another phase is much less known. Here, we examine the fate of defects in an LC confined to a patterned surface during Smectic-A-Nematic and Nematic-Isotropic phase transitions, using experiments and simulation analyses. Upon heating from smectic-A to nematic, a Toric focal conical domain (TFCD) melts into a +1 converging boojum defect, which then transitioned into a concentric configuration as temperature elevates, attributed to a steeper decrease of the bend and twist modulus compared to splay modulus. During cooling, TFCDs are developed from two distinct pathways depending on the cooling rates. Our continuum simulation recapitulates these transformations and provides elastic constants-based explanations of the two pathways. Although the phase transition pathways of defects are independent of the geometry of the confined patterns, the arrangement of FCDs is highly dependent on the size and shape of the patterns. Taken together, this simple approach offers promising opportunities for tuning the micro- or nano-patterning of topological defects in liquid crystals.

Introduction

Liquid crystal materials composed of anisotropic molecules called mesogens are an intriguing system for both fundamental research and practical applications¹. The mesophases of LC formed corresponding to the degree of symmetry given by the arrangement of molecules includes four different phases: nematic (N), smectic (SmA), cholesteric and columnar LCs². When the LC order is broken locally, its director field will generate the topological defects in LCs. The universality of topological defects along with the birefringence property for straightforward characterization using an optical microscope make LCs a model system to study soft matter physics^{3 4}. For example, the disclination lines with 3D structures in blue phase liquid crystals enable the direct capture of martensitic transformation with obvious changes in

color and feature during the phase transition, which is usually hard to observe in solid atomic crystals without sophisticated electron microscopy given to the atomic nature⁴.

Among the various LC phases, the SmA phase possesses a one-dimensional quasi long-range positional order as well as directional order. In SmA phase, the LC molecules are parallel to each other and arranged in layers with thickness close to a few nanometers. The most studied defect in SmA is the so-called focal conic domain (FCD) consisting of an ellipse and hyperbola defect lines in orthogonal planes². In general, the eccentricity of an ellipse between 0 and 1 is observed experimentally. A special case of FCD where eccentricity of ellipse is zero, defined as TFCD, has a straight line passing through its center. Both FCD and TFCD have been studied on

the fabrication of highly ordered LC defect arrays through different methods, such as self-assembly⁵⁻⁹ or external stimuli driven transformations^{6,10,11}. The well-organized arrays of topological defects have been successfully employed in applications, such as particle manipulation^{12,13}, micro lenses^{14,15}, micropattern^{16,17}, and vortex beam generators^{18,19}. So far, most works on SmA LC focused on manipulating and utilizing these SmA LC defects. Only a few studies have revealed the gradual morphological transformation of topological defects during a phase transition²⁰⁻²⁹. The reorganization of LC molecules at the transition point to accommodate the changes in order is an intriguing phenomenon. Recent studies on topological defects appearing in LC spherical shells²⁰⁻²³, LC including colloidal particles^{24,25}, LC thin films on multidirectional rubbed substrate^{26,27}, and LC on water-air interface^{28,29} have identified the morphological changes across the N-SmA transition. The broken directional symmetry of the director $\mathbf{n}(\mathbf{r})$ in N phase is extended to the broken positional symmetry along the \mathbf{n} direction for SmA phase with density modulation to generate equally spaced layers normal to $\mathbf{n}(\mathbf{r})$ ²⁸. The path dependence and defect transformation pathways have been observed during the phase transition²⁹. However, question remains on how the confined patterned surfaces influence the fate of topological defects during phase transitions³⁰. On the other hand, the phase transition of group defects usually occurs in the systems with a large number of defects²⁸. The investigations on the morphology changes of an isolated FCD without the interactions of neighboring defects are rarely reported. The chemically patterned surface provides a facile method to direct defect assembly and observe the evolution of a single defect³¹.

In this work, we analyzed the morphological changes of a single defect during phase transition process, when confined on chemically patterned surfaces. The chemically patterned surface is composed of degenerate planar anchoring regions with pre-designed geometry in a homeotropic anchoring

background, which ensures a single FCD without the influence of the surrounding/neighbor defects. The thermal cycles allow us to reveal the changes in the defect morphology. During the heating process, the TFCD in SmA phase goes through +1 converging boojum defects and to concentric configuration in the N phase. While cooling from the isotropic phase, the defect structure forms a saddle-shape at high cooling speeds, which finally evolves into an FCD. The FCD with eccentricity spontaneously relaxes into TFCD. When the cooling speed was slow, a concentric defect formed on the confined surface, followed by a +1-converging defect, and finally transformed into a TFCD. We related the transformation of defects to the changes of elastic constants through Landau-de Gennes numerical modeling. Meanwhile, we also studied the phase transition process when LCs are confined on the surface with different symmetry of geometrical patterns to reveal the geometrically independent morphological changes observed during thermal treatment. The results reveal the intermediate state of defects and the dependence of the director field on the transformation of defects in LC phases, opening the possibility of using cooling rate to control topological defect structures.

Results and Discussion

The sample fabrication process to achieve self-assembled TFCDs is shown in Fig. 1a. To prepare a chemically patterned surface, a polymer brush poly(6-(4-methoxy-azobenzene-4'-oxy) hexyl methacrylate) PMMAZO was deposited onto the Silicon wafer to form a 3-4 nm thin film after thermal annealing and solvent sonication. Subsequently, a film of e-beam photoresist was spin-coated on top of the polymer brush with a thickness of 60-70 nm. E-beam lithography was used to pattern the photoresist with circular arrays of diameter of 8 μm . The pattern was transferred into the PMMAZO layer through oxygen plasma etching. The removal of photoresist resulted in a patterned substrate with different anchoring behavior contrast due to the presence of PMMAZO brush layer.

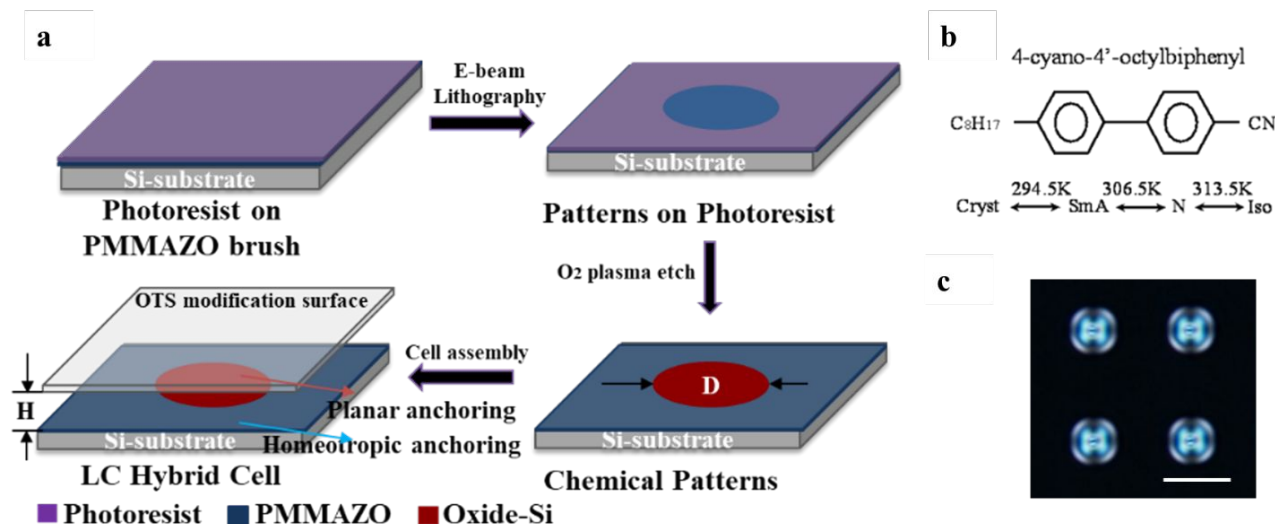


Figure 1. Experimental procedure: a) Schematics of the LC cell preparation with hybrid alignment and chemically patterned substrate. b) 8CB molecular structure and phase transition temperature. c) POM image of the TFCD formation; scalebar: 10 μ m.

The confined region displays degenerate planar anchoring, while the outside area maintains homeotropic anchoring by polymer brush, and the center-to-center distance between two circles is 16 μ m. The sandwich cell with Octadecyltrichlorosilane (OTS) modified glass as top surface was built with $H = 6$ μ m thickness via Mylar spacers. The smectic liquid crystal 4'-Octyl-4-biphenylcarbonitrile (8CB) was injected through capillary action at isotropic temperature to achieve uniform thickness in the cell and then cooled down naturally to room temperature. The phase transition temperature of 8CB used is as follows (Fig. 1b): Crystal to SmA at 21.5 $^{\circ}$ C, SmA to N at 33.5 $^{\circ}$ C and N to Isotropic (I) at 40.5 $^{\circ}$ C. The planar anchoring provided by the confined surfaces on the bottom substrate together with the homeotropic anchoring from top OTS modified glass created a hybrid boundary condition to LC molecules. The Fig. 1c provides a polarizing optical microscopy (POM) image of the LC cell where ordered TFCDs are confined in the circular region isolated from each other. This is a typical TFCD structure with a characteristic Maltese cross pattern. The TFCD is composed of two disclinations: a straight line passing through the center of a circular line. The hybrid boundary conditions facilitate the formation of TFCD where bending of smectic layers on account of a line passing through the center of the circular defect

minimizes the system's free energy. The region outside the TFCDs appears dark under crossed polarizers, because the directors are perpendicular to the crossed polarizers. Here, the confined pattern with different anchoring regions is translated into the presence and absence of TFCDs in an LC cell. The position of TFCD is predetermined and the planar anchoring region limits the size of TFCDs. Therefore, chemically patterned substrate enables the control of the FCD arrangement, in which the position and lateral diameter of the domain can be manipulated to a certain extent. More importantly, without any influence of surrounding defects, morphological transformation of a single defect during phase transition can be revealed in the following research.

To evaluate the defect morphological transition, we investigated the SmA-N-I phase transition of 8CB during heating and cooling cycles. Fig. 2a-d show the change in defect morphology over heating and cooling process, and Fig. 2e-f show the corresponding continuum simulation snapshots of the LC molecular director field for given defect textures (see Simulation Method section). At room temperature, TFCDs are observed when confined in a cell of hybrid anchoring condition. In each TFCD, a series of smectic layer curvatures are accommodated by a straight defect line perpendicular to the substrate, which serves as the

rotational symmetry axis of the TFCD. Close to the bottom substrate inside each circle, the LC molecules

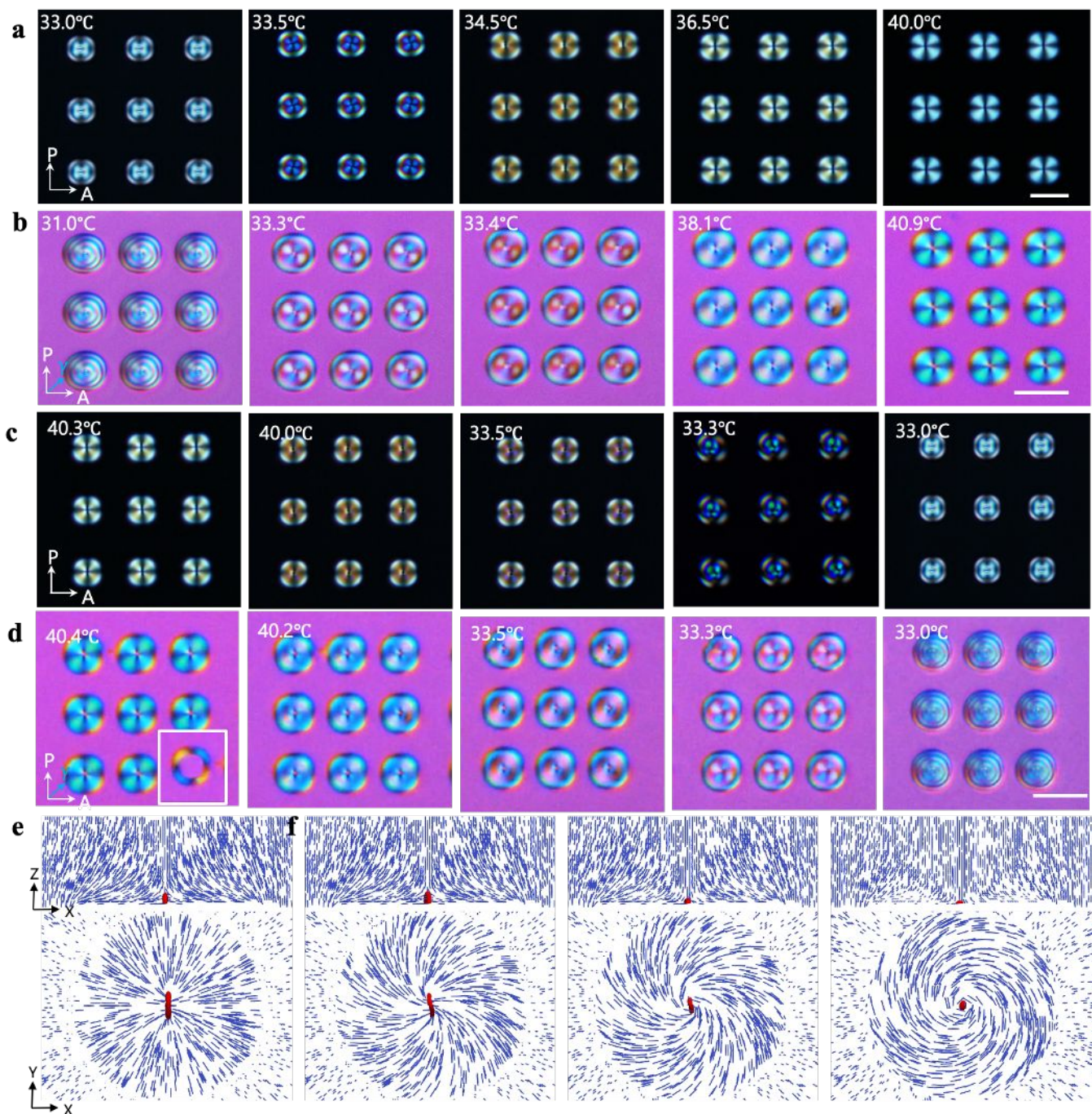


Figure 2. Defect morphology during a heating cycle: a) POM images of defects observed during heating, b) POM images of defects under a retardation plate during the phase transition from SmA-N-Iso, c) POM images of defects observed during cooling, d) POM images of defects under a retardation plate during the phase transition from Iso-N-SmA (Cooling rate: $0.2\text{ }^{\circ}\text{C}/\text{min}$); scalebar: $10\text{ }\mu\text{m}$. e) The director field of +1 converging boojum defects. f) Numerical modeling the transition of +1 converging case to concentric configuration. To trigger the transition, we make the local $\mathbf{n}(\mathbf{r})$ an angle 30° with the radial direction for the initial condition.

are oriented parallel to the bottom surface. When the LC molecules are away from the substrate, splay-bend orientation appears. The delicate balance between the elastic distortions and surface anchoring produces a stable TFCD. When provided sufficient thermal energy for the transition from SmA to N phase at 33.5 °C, the TFCD transforms into a +1 boojum defect with converging directors (Fig. 2a). Then, the local symmetry broken, with right- and left-handed twists forming on each circle and the occurrence of right- or left-handed was random. The +1 boojum defects are visualized as four dark and four bright branches intersecting at a point. Here, the schlieren texture generates defects of topological charge s when the number of branches at a point is four times the absolute value of s . The sign of s is determined by rotating the crossed polarizer. The rotation of the branches either in the same or opposite direction of the rotation, gives a positive or negative sign, respectively. Further increasing temperature to input thermal energy, the +1 converging boojum defects gradually transits into the concentric conformation in N phase, where the director field aligns in the direction tangent to the confined circles with bend distortions (Fig. 2f). This transition is attributed to the

rapid decrease of the bend modulus, as the elastic constant of bending is close to that of splay when the temperature is above 34.5 °C. The transition of the concentric configuration seen from 34.5 °C to 40 °C can be analyzed using Michel–Lévy interference chart where the transition in interference colors reflects the wavelength³². With increasing temperature from the N phase to I phase the change of interference colors from deep red to orange to yellow and white is observed. The transition color series indicates that this is a first order phase transition.

To further understand the first order transition observed when heating the sample from SmA phase to isotropic phase, a first order retardation plate ($\lambda = 530$ nm) was introduced to convert the director orientations with color difference (Fig. 2b). When the director \mathbf{n} is parallel or perpendicular to the polarizer, the magenta color appears; while for the director parallel or perpendicular to the slow axis of the retardation plate, yellow and blue appear, respectively. In the SmA phase, the TFCDs with stacked layers of LC molecules arranged on top of one another can be visualized through the retardation plate. In the N phase, the region around the defect core

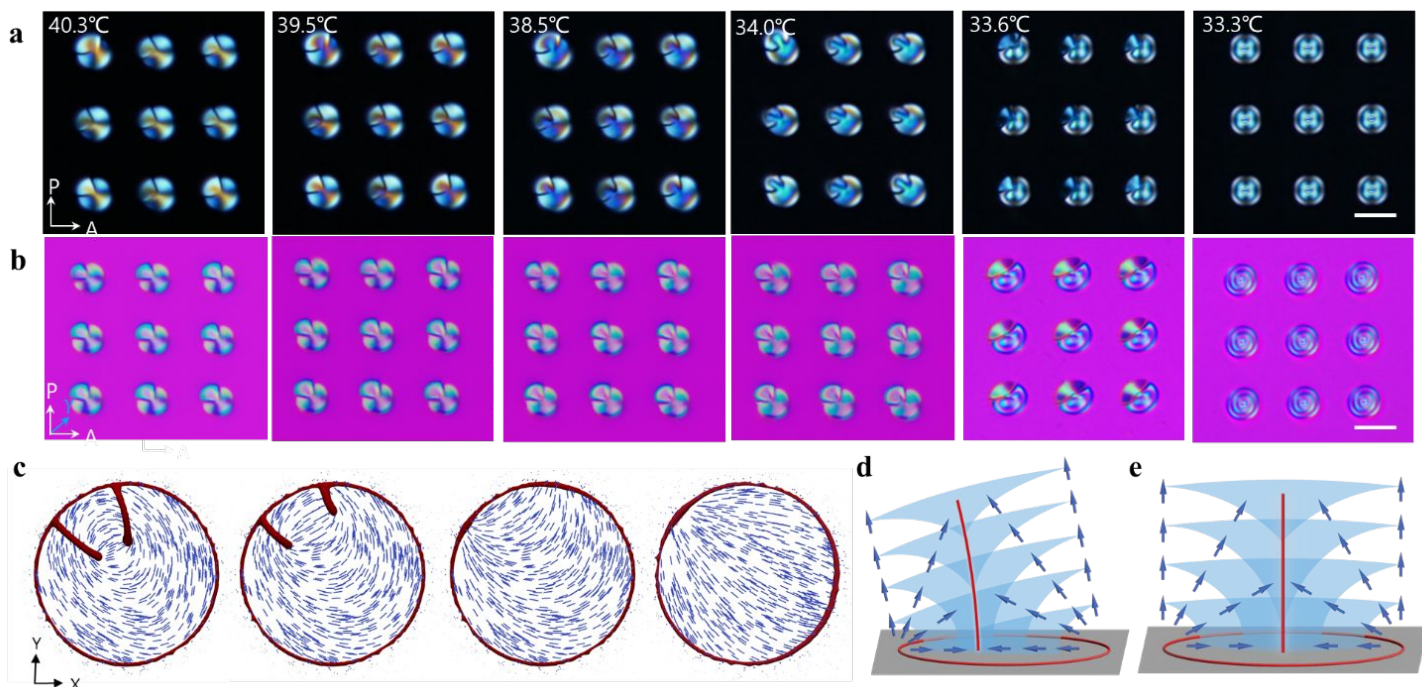


Figure 3. Defect morphology during a rapid cooling cycle: a) POM images of defects observed during cooling from Iso-N-SmA phase (Cooling rate: 0.7 °C/min). b) POM images of defects under a retardation plate during the phase transition from Iso-N-SmA (Cooling rate: 0.7 °C/min); Scalebar: 10 μ m. c) Numerical simulation of the transition from saddle shape defects to boojum structure. The initial condition is the saddle shape defect. During evolution, K_{33} increased continuously from 2 to 6, while K_{22} and K_{11} remained constant. d) FCD with high value of eccentricity, and e) TFCD with zero eccentricity.

exhibit two yellow lobes outlined with a magenta meeting at the center. A faded yellow spot is observed, which corresponds to a nematic radial conjuring molecules in an up or down direction corresponding to the normal of the substrate to give converging or diverging radial. The transition to concentric configuration can be observed through a gradual change of the color to cyan blue over the whole area.

The phase transition morphologies observed while cooling from I to SmA phase were divided into two categories regarding the cooling rate. For slow cooling rate, *i.e.*, $0.2\text{ }^\circ\text{C}/\text{min}$, the defect transition observed is shown in Fig. 2c-d. The circular confinement of defect morphology can be confirmed via the inset image shown at $40.4\text{ }^\circ\text{C}$ in Fig. 2d. With slow cooling rate the gradual transition of defect morphology from concentric configuration to the +1 converging radials in N phase is seen, which is quite similar to the reverse of the heating cycle observations. Further cooling from nematic to SmA phase, the +1 converging defects transformed into TFCDs. The identical phase transition behavior during cooling cycle is detected for the cooling rate below $0.5\text{ }^\circ\text{C}/\text{min}$.

Continuum simulation based on Landau–de Gennes free energy functional provides a reasonable way to study the transformation of +1 converging boojum defects in the N phase. Homeotropic anchoring is imposed on the bottom and top surface, and degenerate planar anchoring is imposed on the confined circular region. The anchoring strength is strong but finite. The director field of the initial condition matches the +1 converging cases with some degrees of twist (Fig. 2e). Near the SmA-N phase transition point, the bend (K_{33}) and twist moduli (K_{22}) diverge, compared to splay modulus remaining finite³³. Thus, the +1 converging boojum configuration is energetically favorable. In N phase, the ratio between K_{33} and K_{11} is close to 1, and the cost of bending distortion becomes cheaper when away from the SmA-N transition point. By setting the elastic constant $K_{33} = K_{11}$, the +1 converging boojum defect configuration with directors making an angle 30° with the radial direction, directly translated into the concentric configuration (Fig. 2f). This calculation correctly captures the transition of the director configuration in the experiment.

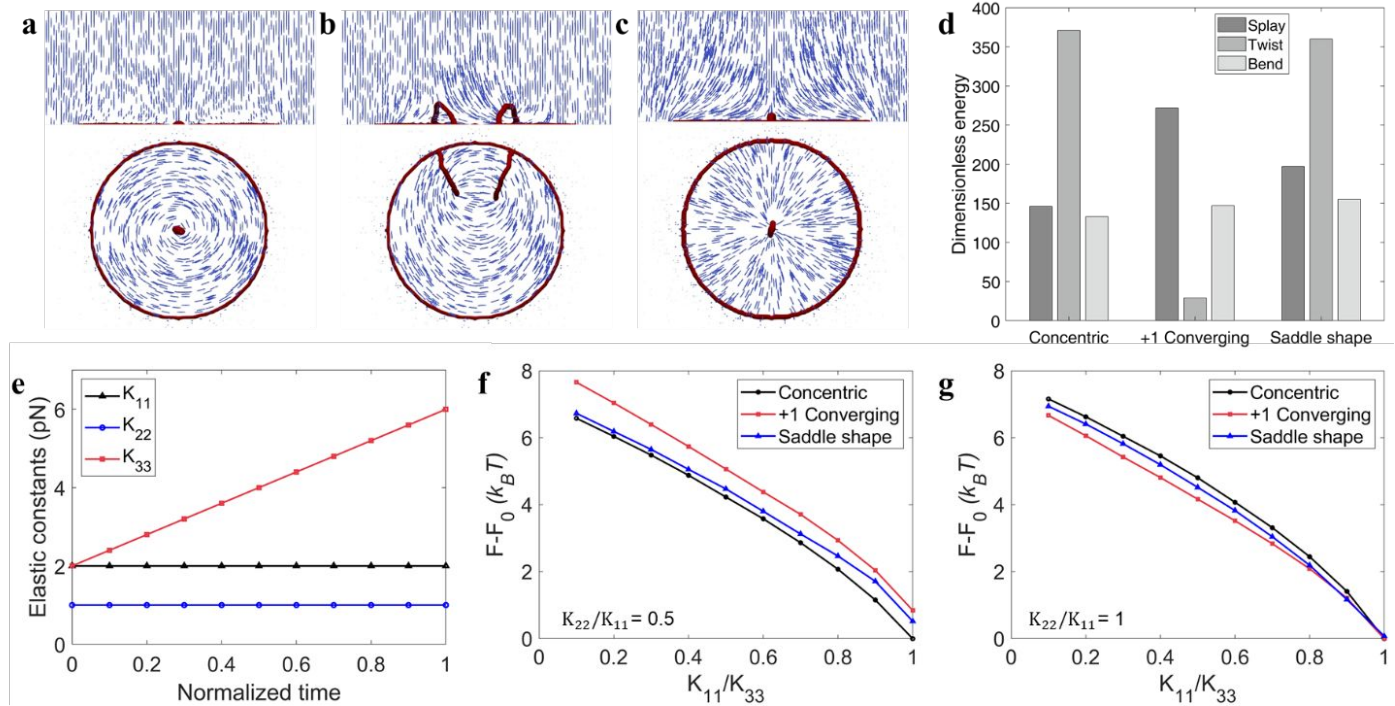


Figure 4. Simulated director configurations and defects stability. a-c) Stationary liquid crystal configurations *i.e.*, concentric a), saddle shape defect b) and +1 converging c) with a side and a top view. d) Free energy of each deformation mode. e) Elastic constants as functions of evolution time for the simulation in Fig. 2c. The total free energy curve of the director configurations with respect to the ratio K_{11}/K_{33} , for $K_{22} = 0.5K_{11}$ f) and $K_{22} = K_{11}$ g).

In contrast to the slow cooling rate the phase transition during rapid cooling with a rate of $0.7\text{ }^{\circ}\text{C}/\text{min}$ reveals a distinct pathway. Two morphological stages occur (Fig. 3a-b): in the N phase, the saddle shape defects transformed into boojum defects; whereas the transition at N-SmA phase, a fan-shaped lobe evolved from the boojum defect and finally developed into a FCD with high eccentricity. When cooling down ($0.7\text{ }^{\circ}\text{C}/\text{min}$) from the isotropic phase, randomly oriented LC molecules transit into nematic phase with

the cost of bending and twist became high, the system evolved into a boojum structure³⁴.

At the phase transition temperature of N - SmA, the FCD with a high value of eccentricity nucleates from the boojum structure. The observed FCD, with a negative Gaussian curvature, is composed of two defect lines, the confocal ellipse and the hyperbola lying in the planes orthogonal to each other (Fig. 3d). The FCD observed can be described in terms of the eccentricity value of elliptical defect line $e =$

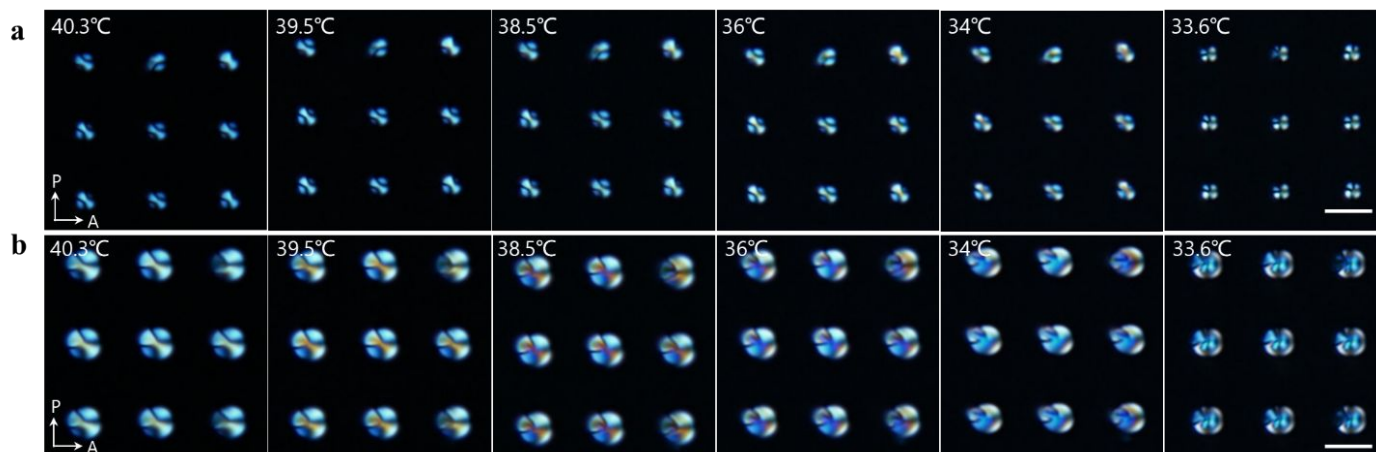


Figure 5. Confinement effect: POM images of LC cooling down from Iso-SmA phase (Cooling rate: $0.7\text{ }^{\circ}\text{C}/\text{min}$) when confined in circle with diameter a) $4\text{ }\mu\text{m}$ and b) $7\text{ }\mu\text{m}$, scalebar: $10\text{ }\mu\text{m}$.

splay bend conformation. Inside the planar circle, the saddle-shape morphological defect developed from one end of the circle along the 45° corresponding to the crossed polarizer to the other end. Fig. 3b displays the retardation plate data while cooling down from I phase to SmA phase. The director's orientation around the outer layer was in the circumferential directions. The continuum simulation revealed the changes in defects configuration during phase transition. When quenched to the nematic phase, two disclinations formed, each connecting a $+1/2$ defect and the periphery of the circular pattern (Fig. 3c), also indicated by the POM images (saddle shape defects). Because of the rapid cooling, the system did not have sufficient time to relax to the concentric state observed in the slow cooling process. It adapted to a multi-stable state, the saddle shape defect, in N phase. With the evolution of the system, the two disclinations moved to the periphery, and eliminated. There still existed bending distortions due to the low cost of bending. When the temperature was further decreased,

$\sqrt{1 - b^2/a^2}$ with the semi-major axis a and the semi-minor axis b . Experimentally eccentricity values in the range of $0 \leq e < 1$ can be observed. FCDs with nonzero eccentricity are termed as elliptic-hyperbolic FCDs. As the SmA phase is cooled, the eccentricity value is lowered and only a quarter of FCD is obscured. Finally, the elliptic-hyperbolic FCD transforms into the TFCD ($e = 0$), where a circle disclination is generated instead of an elliptical one (Fig. 3e).

The three configurations, *i.e.*, $+1$ converging, saddle shape and concentric configuration, may be favored depending on the combination of elastic constants. The relative stability is mainly determined by the distortion at the top of the confined pattern (Fig. 4a-c). Fig. 4d shows that twist distortion of $+1$ converging configuration is much smaller than that of concentric and saddle shape configuration. At the N-SmA phase transition point, as K_{22} diverges, the $+1$ converging configuration is energetically favorable. Then, as a function of K_{11}/K_{33} , we test the stability of three configurations observed in the experiments by

calculating their total free energy. In nematic state, when K_{22} is relatively small, the concentric configuration is the stable state (Fig. 4f). Whereas a larger K_{22} makes the +1 converging configuration stable (Fig. 4g). Note that the saddle shape configuration is a metastable state, independent of the magnitude of K_{22} in our calculations. This is consistent with the observation of this configuration during fast cooling experiments. The calculations indicate that temperature-dependent K_{22} plays a key role in driving the transition between concentric and +1 converging configuration.

Considering the effect of dimension of the confined area on the phase transition, circles with diameters ranging from 1 μm to 8 μm were studied during rapid cooling (0.7 $^{\circ}\text{C}/\text{min}$) from Iso to SmA phase. Fig. 5 displays the POM images of 8CB confined in circles with diameter of 4 μm (Fig. 5a) and 7 μm (Fig. 5b) as the temperature falls to N phase. For the circular confinement with a diameter of 4 μm , the saddle-shape defect structure is noticed right after Iso-N phase transition and is locked in until the N-SmA temperature is reached. However, under the larger circular confinement, the saddle-shape morphs into a lobe at the corner in the N phase at 36 $^{\circ}\text{C}$. With further cooling to 34 $^{\circ}\text{C}$, FCD with high eccentricity, at N-SmA phase transition, is generated. Different than the saddle-shape defects in 4 μm diameter circle, when the diameter of circle is above 4 μm , the saddle-shaped defect structure does not stabilize over the entire N phase temperature. Increasing the diameter of circle above 4 μm lowers the range of temperature over which the saddle-shape defect is observed. Whereas further reducing the diameter below 4 μm , the LC defect follows the similar fate as observed under the 4 μm diameter circle. Albeit the dimension of confined area affects the stable state of defects in nematic phase, the phase transition still follows the same pathways: saddle shape defects form in N phase and transform into FCD in SmA phase.

The surface pattern constrains the layer structure of liquid crystals to follow its geometry and deform themselves into a stable defect morphology in SmA phase. Circular confinement has a higher symmetry than other geometries. To investigate the phase transition when confined in geometry with lower

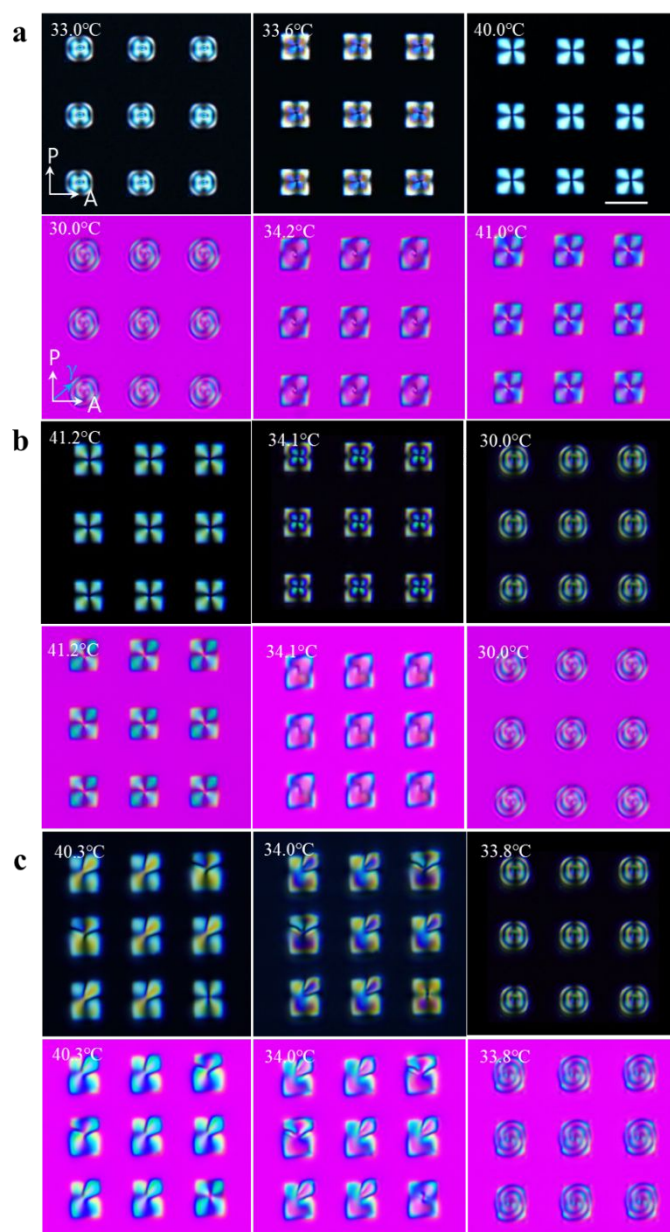


Figure 6. Geometric independence: POM images of defect morphological transition observed when 8CB confined in patterns with square geometry during heating a), slow cooling (Cooling rate: 0.2 $^{\circ}\text{C}/\text{min}$) b), and rapid cooling (Cooling rate: 0.7 $^{\circ}\text{C}/\text{min}$) c); scalebar: 10 μm

symmetry, a surface pattern with square geometry was fabricated. As a consequence of four edges with equal size at an angle of 90 $^{\circ}$, the square geometry contains four lines of symmetry. The square pattern with 7 \times 7 μm^2 dimensions, formed a single TFCd in the pattern region at room temperature. The confined LC morphology transformations on this surface were also studied under heating and cooling cycles. By heating the sample, the TFCds transitioned to +1 converging

boojum defects at SmA-N phase transition, and then the defects gradually morphed into concentric configuration before reaching the isotropic phase (Fig. 6a). The defects observed during rapid and slow cooling rates show similar development as in the circular geometry. For slow cooling rate ($0.2\text{ }^{\circ}\text{C}/\text{min}$) the transition of concentric conformation to nematic radial with +1 value is noticed, as seen in Fig. 6b. When cooling down to SmA phase, a TFCD, the ground, is generated. While the higher cooling rate ($0.7\text{ }^{\circ}\text{C}/\text{min}$) presents saddle-shape morphology transitioning to FCD with eccentricity and finally reaching the TFCD (Fig. 6c). Although the direction of saddle-shape originated in square confinement is different from the circular confinement, their paths of phase transition are identical. These results suggest that the phase transition pathways observed are independent of the symmetry of the confinement surface geometry.

Next, the length of the rectangular pattern varied from $1\text{ }\mu\text{m}$ to $16\text{ }\mu\text{m}$, while keeping the width constant at $7\text{ }\mu\text{m}$, in order to investigate the influence of the patterns' size on the formation of FCDs. Fig. 7 displays the POM images and a plot representing the change in FCD dimensions with increasing length of rectangular pattern. When the length of the rectangle is below $5\text{ }\mu\text{m}$, multiple FCDs with smaller sizes are trapped in the patterned area. Here, increasing length from $1\text{ }\mu\text{m}$ to $5\text{ }\mu\text{m}$ reduced the number of TFCDs occupying the patterned area (Fig. 7a). The size of TFCDs in area experienced an increase from 1 to $3\text{ }\mu\text{m}$ when coupled with an increase in the length of the pattern. For the length set at $5\text{ }\mu\text{m}$ a single TFCD formed inside the rectangle with width $6\text{ }\mu\text{m}$ and length $4.5\text{ }\mu\text{m}$ respectively. As the length of the pattern stepped up to $8\text{ }\mu\text{m}$, the width of TFCD also

consequently changed from 6 to $6.5\text{ }\mu\text{m}$ and length from 4.5 to $7.4\text{ }\mu\text{m}$. Above $9\text{ }\mu\text{m}$ length, as seen in the POM images, the TFCD starts splitting, and subsequently another FCD emerges as the length is increased ($L = 10\text{ }\mu\text{m}$). After splitting the initial TFCD, a second FCD emerged and shows eccentricity. When the pattern with length $11\text{ }\mu\text{m}$ and width $7\text{ }\mu\text{m}$ is studied, two TFCDs with equal size (width = $6.5\text{ }\mu\text{m}$, length = $5\text{ }\mu\text{m}$) are observed in the confined area. Beyond $11\text{ }\mu\text{m}$ length of the pattern, the width of TFCDs confined remained similar. However, the length of TFCDs adapted and increased according to the length of confined pattern. It's clear that the smaller dimensional value controls the FCD domains confined in the pattern region. Beyond certain dimensions, instead of varying the FCD size to full fill the planner anchoring region, the FCDs generate more FCDs. As the TFCD occupies the area of confined

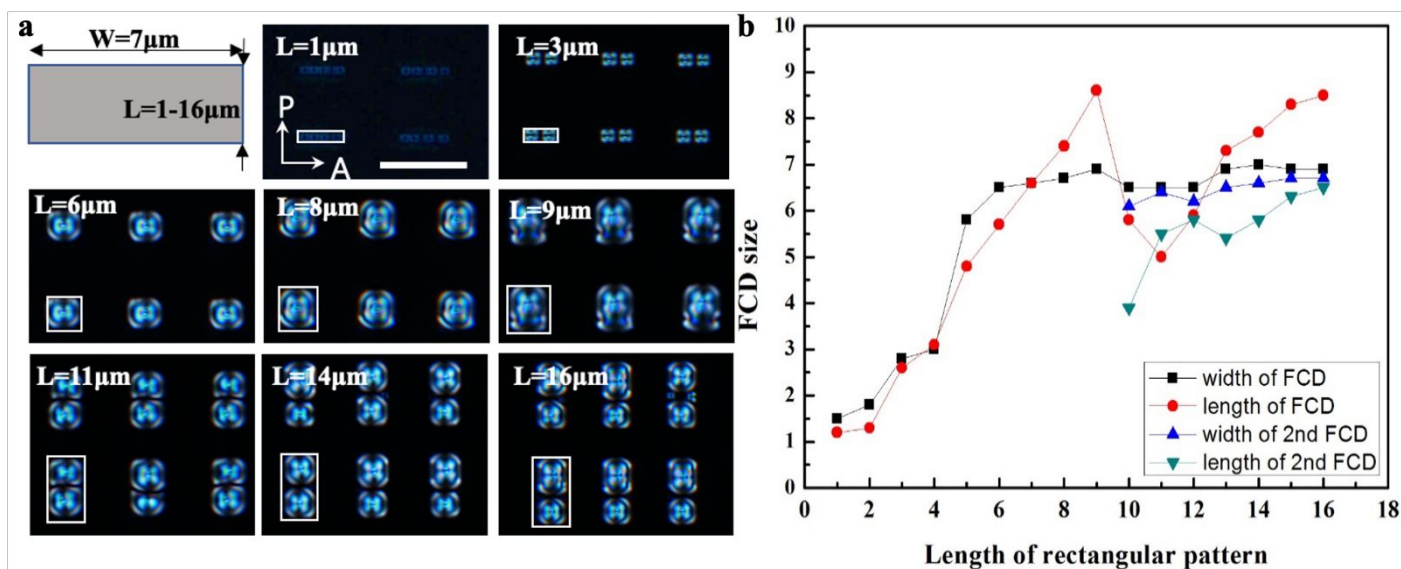


Figure 7. The size dependence of FCD: a) POM images of FCD confined in pattern with constant width of $7\text{ }\mu\text{m}$ and varying length from $1\text{ }\mu\text{m}$ to $16\text{ }\mu\text{m}$ for cell thickness $6\text{ }\mu\text{m}$; scale bar: $20\text{ }\mu\text{m}$. b) Plot of FCD dimension i.e., width and length with change in length of rectangular pattern.

pattern to minimize the total energy of the area rather than a single TFCD³⁵. The plot in Fig. 7b tracks the length and width of FCD versus the length of the rectangular pattern. From the plot it's clear that increasing the length of the pattern affected the dimensions of FCDs trapped in the pattern. The plot also accounts for the size of the second FCD generated while increasing the length of rectangle.

Conclusion:

Using the confined chemically patterned surface, we have demonstrated two distinct pathways of defect transformation during phase transitions: a direct conversion of TFCD to a +1 converging boojum defect which finally transformed into concentric configuration during heating and, depending on the cooling rate, a sequence of morphological transformations from saddle-shape defect to FCDs, finally to TFCD in the fast-cooling process. The phase transition pathways are independent of the symmetry of the confined patterns, while the arrangement of TFCD is highly influenced by the shape and size of the patterns. When the ratio between the length and width of the rectangular pattern is higher than 1.2, the FCD will split into two or more FCDs. Meanwhile, there is still a need for the systematically experimental, theoretical, and computational investigation of how the shape and size of confined patterns influence the arrangement of FCDs in SmA phase. The dynamics of multiple FCDs forming on a predesigned pattern are also interesting for future study. Our findings encourage investigation into phase transition pathways, self-assembly and micro-patterning.

Experimental section:

Materials. The thermotropic 4-cyano-4'-octylbiphenyl (8CB) liquid crystal was purchased from Sigma-Aldrich and used for the experimental and theoretical analysis. 8CB exhibits a smectic A phase between 21.5 to 33.5 °C and nematic phase between 33.5 to 40.5 °C. Octadecyltrichlorosilane (OTS), heptane, chlorobenzene, isopropyl alcohol (IPA) and dichloromethane (DCM) were purchased from Sigma-Aldrich. The LC polymer brush PMMAZO, poly (6-(4-methoxy-azobenzene-4'-oxy) hexyl methacrylate) was synthesized through process

reported by Stewart and Imrie. Glass microscope slides with finest premium grade were purchased from Fisher Scientific.

Preparation of PMMAZO brush chemical patterns. A PMMAZO film was deposited on a piranha cleaned silicon substrate by spin-coating a 0.05 wt% chlorobenzene solution at 4000 rpm for 60 s and annealed at 250 °C for 5 min under nitrogen atmosphere. The Non-grafted PMMAZO was removed by sonication in chlorobenzene three times for 5 minutes and the remaining PMMAZO brush was found to be around 3-4 nm.

A 40 nm-thick GL2000 photoresist film was spin-coated onto the PMMAZO brush and baked at 160 °C for 5 min. Patterns with an array of circular, triangular, and square shapes were exposed on the resists using electron beam lithography with the JEOL 9300FS electron-beam writer at the Center for Nanoscale Materials, Argonne National Laboratory. The Exposed substrates were developed in n-amyl acetate for 15 s followed by rinse with isopropyl alcohol. The oxygen plasma etching transformed the resulting resist pattern onto a chemical pattern on the PMMAZO brush layer, followed by stripping the GL2000 photoresist in chlorobenzene through sonication.

Preparation of optical cells. The glass microscope slides were boiled in a piranha solution (7:3 (v/v) of 98% H₂SO₄/30% H₂O₂) at 130 °C for 1 hour, to remove any stains on the surface, followed by wash with DI water and drying with nitrogen. For OTS modification, the cleaned glass slides were immersed in a mixture of 13.8 μL OTS and 120 ml heptane for 1 hour. Afterwards, the slides were removed from the solution and washed with DCM two times then quickly dried under a nitrogen flow. The OTS glass and the Si substrate with the PMMAZO substrate were placed face-to-face, with a 6 μm spacer, to create a cell. The optical cell and the LC were heated above the clearing point and 8CB was injected through capillary action. The system was then slowly cooled down to room temperature.

Characterization. The thickness of the PMMAZO brush was measured by a Woollam VUV-VASE32 variable angle spectroscopic ellipsometer. The JEOL

9300FS electron-beam writer at Center for Nanoscale Materials, Argonne National Laboratory was used to write chemical patterns. The optical images of the LC cell were obtained with a BX 60 Olympus polarized light microscope.

Numerical methods. The nematic configuration is described by a traceless and symmetric tensor, defined as: $Q_{ij} = q(n_i n_j - \frac{1}{3}\delta_{ij})$, where q is the scalar order parameter, \mathbf{n} is a unit vector representing the nematic orientation. The free energy, F , of the nematic liquid crystal is expressed as follow³⁶⁻³⁸:

$$F = \int_V dV f_{bulk} + \int_{\partial V} dV f_{surface} = \int_V dV (f_{LDG} + f_{el}) + \int_{\partial V} dV f_{surface}, \quad (1)$$

where the bulk energy is composed of a long-range elastic energy density f_{el} and a short-range free energy density f_{LDG} . The surface energy $f_{surface}$ is caused by the anchoring. The phase energy densities f_{LDG} is expressed as the following form³⁶:

$$f_{LDG} = \frac{A_0}{2} \left(1 - \frac{U}{3}\right) \text{Tr}(Q^2) - \frac{A_0 U}{3} \text{Tr}(Q^3) + \frac{A_0 U}{4} \text{Tr}(Q^2)^2. \quad (2)$$

Parameter U controls the magnitude of q_0 , the equilibrium scalar order parameter via $q_0 = \frac{1}{4} + \frac{3}{4} \sqrt{1 - \frac{8}{3U}}$. The elastic energy densities f_{el} is given by an expression of the form ($Q_{ij,k}$, which means $\partial_k Q_{ij}$):

$$f_{el} = \frac{1}{2} L_1 Q_{ij,k} Q_{ij,k} + \frac{1}{2} L_2 Q_{ij,j} Q_{ik,k} + \frac{1}{2} L_3 Q_{ij} Q_{kl,i} Q_{kl,j} + \frac{1}{2} L_4 Q_{ik,l} Q_{il,k}, \quad (3)$$

When the system is uniaxial, in Eq.3, the L 's can be mapped to the Frank elastic constants by: $L_1 = \frac{1}{2q_0^2}$

$\left[K_{22} + \frac{1}{3}(K_{33} - K_{11}) \right]$, $L_2 = \frac{1}{q_0^2}(K_{11} - K_{24})$, $L_3 = \frac{1}{2q_0^2}(K_{33} - K_{11})$, $L_4 = \frac{1}{q_0^2}(K_{24} - K_{22})$. In the anchoring energy density, $f_{surface}$, homeotropic anchoring is modeled through a Rapini-Papoular expression: $f_{surface} = \frac{1}{2} W (Q - Q_0)^2$, where Q_0 is the surface preferred Q -tensor. Degenerate planar anchoring is modeled based on the form: $f_{surface} = W (\tilde{Q} - \tilde{Q}^\perp)^2$, where $\tilde{Q}_{ij} = Q_{ij} + \frac{1}{3} q_0 \delta_{ij}$, using the projection operator: $\tilde{Q}_{ij}^\perp = P_{ik} \tilde{Q}_{kl} P_{lj}$, $P_{ij} = \delta_{ij} - v_i v_j$. The tensor P_{ij} subtracts out the normal of the Q -tensor and \mathbf{v} is the substrate normal.

Numerical details. The free energy F is minimized according to Euler Lagrange equation solved by a finite difference method. The units are chosen as follows: $A_0 = 1$, $U = 3.5$, leading to $q_0 \cong 0.62$. The homeotropic anchoring strengths for top surface and bottom surface are 0.1 and 0.01, respectively. The value for the planar anchoring strength on the confined area is set to be 1. For the numerical process of transition from +1 converging configuration to concentric configuration in Fig. 2e, the initial condition is a +1-converging configuration with a left-handed twist and $q = q_0$ everywhere. We keep $K_{11} = 2$, $K_{22} = 1$, $K_{33} = 2$, $K_{24} = 1$. In Fig. 3c, for the initial condition, there are two disclinations connecting the $+1/2$ defects and the periphery. We increased the K_{33} from 2 to 6 during the minimization of free energy to simulate the cooling process, while other Frank elastic constants were kept constant and the same as the abovementioned one (Fig. 4e). The simulation is performed on a square lattice with periodic boundary conditions in two lateral directions.

AUTHOR INFORMATION

Corresponding Author

*E-mail: Xiao.Li@unt.edu, ruizhang@ust.hk

Author contributions

X.L. conceived and designed the experiments. T.P. and X.W. performed the experiments. R.Z. conceived and designed the simulations. S.Z. and R.Z. performed the simulations. T.P., S.Z., R.Z. and X.L. wrote the manuscript. X.L. and R.Z. guided the work. All authors discussed the results and contributed to data analysis and manuscript revision.

ACKNOWLEDGMENT

We gratefully acknowledge support of startup funding from University of North Texas. We acknowledge the use of the facility resources provided by the Center for Nanoscale Materials, a U. S. Department of Energy (DOE) Office of Science User Facility operated for the DOE Office of Science by Argonne National Laboratory under Contract No. DE-AC02-06CH11357, and University of North Texas' Materials Research Facility. R.Z. acknowledges the financial support from Hong Kong Research Grants Council no. 16300221. R.Z. thanks Daniel Beller for helpful discussions.

References

- 1 Q. Li, *Nanoscience with Liquid Crystals From Self-Organized Nanostructures to Applications*, 2014.
- 2 M. Kleman, *Reports on progress in physics*, 1989, **52**, 555-654 (DOI:10.1088/0034-4885/52/5/002).
- 3 B. Zappone, A. E. Mamuk, I. Gryn, V. Arima, A. Zizzari, R. Bartolino, E. Lacaze and R. Petschek, *Proceedings of the National Academy of Sciences - PNAS*, 2020, **117**, 17643-17649 (DOI:10.1073/pnas.2000849117).
- 4 X. Li, J. A. Martínez-González, J. P. Hernández-Ortiz, A. Ramírez-Hernández, Y. Zhou, M. Sadati, R. Zhang, P. F. Nealey and J. J. de Pablo, *Proceedings of the National Academy of Sciences - PNAS*, 2017, **114**, 10011-10016 (DOI:10.1073/pnas.1711207114).
- 5 T. Araki, F. Serra and H. Tanaka, *Soft matter*, 2013, **9**, 817-812 (DOI:10.1039/c3sm50468a).
- 6 A. Suh, H. Ahn, T. J. Shin and D. K. Yoon, *Journal of materials chemistry. C, Materials for optical and electronic devices*, 2019, **7**, 1713-1719 (DOI:10.1039/C8TC06042H).
- 7 S. Wu, L. Ma, P. Chen, H. Cao, S. Ge, R. Yuan, W. Hu and Y. Lu, *Advanced optical materials*, 2020, **8**, 2000593-n/a (DOI:10.1002/adom.202000593).
- 8 A. Honglawan, D. A. Beller, J. Cavallaro Marcello, R. D. Kamien, K. J. Stebe and S. Yang, *Proceedings of the National Academy of Sciences - PNAS*, 2013, **110**, 34-39 (DOI:10.1073/pnas.1214708109).
- 9 D. S. Kim, S. Čopar, U. Tkalec and D. K. Yoon, *Science advances*, 2018, **4** (DOI:10.1126/sciadv.aau8064).
- 10 R. You, Y. Choi, M. J. Shin, M. Seo and D. K. Yoon, *Advanced materials technologies*, 2019, **4**, 1900454-n/a (DOI:10.1002/admt.201900454).
- 11 M. J. Shin and D. K. Yoon, *Materials*, 2020, **13**, 5466 (DOI:10.3390/ma13235466).
- 12 I. Musevic, M. Skarabot, U. Tkalec, M. Ravnik and S. Zumer, *Science*, 2006, **313**, 954-958 (DOI:10.1126/science.1129660).
- 13 H. Jung, D. K. Yoon, M. C. Choi, Y. H. Kim, M. W. Kim and O. D. Lavrentovich, *Nature materials*, 2007, **6**, 866-870 (DOI:10.1038/nmat2029).
- 14 Y. H. Kim, H. S. Jeong, J. H. Kim, E. K. Yoon, D. K. Yoon and H. Jung, *Journal of materials chemistry*, 2010, **20**, 6557 (DOI:10.1039/c0jm00910e).
- 15 F. Serra, M. A. Gharbi, Y. Luo, I. B. Liu, N. D. Bade, R. D. Kamien, S. Yang and K. J. Stebe, *Advanced optical materials*, 2015, **3**, 1287-1292 (DOI:10.1002/adom.201500153).

- 16 Y. H. Kim, D. K. Yoon, H. S. Jeong and H. Jung, *Soft matter*, 2010, **6**, 1426 (DOI:10.1039/b924401h).
- 17 Y. H. Kim, J. Lee, H. S. Jeong, J. H. Kim, E. K. Yoon, D. K. Yoon, J. Yoon and H. Jung, *Advanced materials (Weinheim)*, 2010, **22**, 2416-2420 (DOI:10.1002/adma.200903728).
- 18 R. Barboza, U. Bortolozzo, G. Assanto, E. Vidal-Henriquez, M. G. Clerc and S. Residori, *Physical Review Letters*, 2013, **111**.
- 19 B. Son, S. Kim, Y. H. Kim, K. Kälántár, H. Kim, H. Jeong, S. Q. Choi, J. Shin, H. Jung and Y. Lee, *Optics express*, 2014, **22**, 4699-4704 (DOI:10.1364/OE.22.004699).
- 20 H. Liang, S. Schymura, P. Rudquist and J. Lagerwall, *Physical review letters*, 2011, **106**, 247801 (DOI:10.1103/PhysRevLett.106.247801).
- 21 T. Lopez-Leon, A. Fernandez-Nieves, M. Nobili and C. Blanc, *J.Phys.CM*, 2012, **24**, 284122 (DOI:10.1088/0953-8984/24/28/284122).
- 22 T. Lopez-Leon, A. Fernandez-Nieves, M. Nobili and C. Blanc, *Physical review letters*, 2011, **106**, 247802 (DOI:10.1103/PhysRevLett.106.247802).
- 23 H. Liang, J. Noh, R. Zentel, P. Rudquist and J. P. F. Lagerwall, *Philosophical transactions of the Royal Society of London. Series A: Mathematical, physical, and engineering sciences*, 2013, **371**, 20120258 (DOI:10.1098/rsta.2012.0258).
- 24 K. P. Zuhail, P. Sathyanarayana, D. Seč, S. Čopar, M. Škarabot, I. Muševič and S. Dhara, *Physical review. E, Statistical, nonlinear, and soft matter physics*, 2015, **91**, 030501.
- 25 K. P. Zuhail and S. Dhara, *Soft matter*, 2016, **12**, 6812-6816 (DOI:10.1039/C6SM01244B).
- 26 J. M. Ok, Y. H. Kim, T. Y. Lee, H. Yoo, K. Kwon, W. Jung, S. Kim and H. Jung, *Langmuir*, 2016, **32**, 13418-13426 (DOI:10.1021/acs.langmuir.6b03355).
- 27 J. M. Ok, Y. H. Kim, H. S. Jeong, H. Yoo, J. H. Kim, M. Srinivasarao and H. Jung, *Soft matter*, 2013, **9**, 10135 (DOI:10.1039/c3sm52008k).
- 28 M. Gim, D. A. Beller and D. K. Yoon, *Nature communications*, 2017, **8**, 15453 (DOI:10.1038/ncomms15453).
- 29 A. Suh, M. Gim, D. Beller and D. K. Yoon, *Soft matter*, 2019, **15**, 5835-5841 (DOI:10.1039/C9SM00781D).
- 30 S. H. Ryu and D. K. Yoon, *Liquid crystals*, 2016, **43**, 1951-1972 (DOI:10.1080/02678292.2016.1205674).
- 31 J. P. Bramble, S. D. Evans, J. R. Henderson, T. J. Atherton and N. J. Smith, *Liquid crystals*, 2007, **34**, 1137-1143 (DOI:10.1080/02678290701618351).
- 32 B. E. Sorensen, *European journal of mineralogy (Stuttgart)*, 2013, **25**, 5-10 (DOI:10.1127/0935-1221/2013/0025-2252).
- 33 N. V. Madhusudana and R. Pratibha, *Molecular crystals and liquid crystals (1969)*, 1982, **89**, 249-257 (DOI:10.1080/00268948208074481).
- 34 Y. Xia, A. A. DeBenedictis, D. S. Kim, S. Chen, S. Kim, D. J. Cleaver, T. J. Atherton and S. Yang, *Nature communications*, 2019, **10**, 5104-9 (DOI:10.1038/s41467-019-13012-9).
- 35 C. Blanc and M. Kleman, *Physical review. E, Statistical physics, plasmas, fluids, and related interdisciplinary topics*, 2000, **62**, 6739-6748 (DOI:10.1103/PhysRevE.62.6739).
- 36 M. Ravnik and S. Žumer, *Liquid crystals*, 2009, **36**, 1201-1214 (DOI:10.1080/02678290903056095).

37 N. Kumar, R. Zhang, J. J. de Pablo and M. L. Gardel, *Science advances*, 2018, **4**, eaat7779 (DOI:10.1126/sciadv.aat7779).

38 R. Zhang, S. A. Redford, P. V. Ruijgrok, N. Kumar, A. Mozaffari, S. Zemsky, A. R. Dinner, V. Vitelli, Z. Bryant, M. L. Gardel and J. J. de Pablo, *Nature materials*, 2021, **20**, 875-882 (DOI:10.1038/s41563-020-00901-4).